Mechanics of Materials 94 (2016) 53–65

Contents lists available at ScienceDirect

Mechanics of Materials

journal homepage: www.elsevier.com/locate/mechmat

Materials based design of structures: Computational modeling of the mechanical behavior of gold-polymer nanocomposites

Swantje Bargmann[a,b,*], Celal Soyarslan[a], Edgar Husser[b], Natalia Konchakova[a]

[a] Institute of Continuum Mechanics and Material Mechanics, Hamburg University of Technology, Eißendorfer Str. 42, 21073 Hamburg, Germany
[b] Institute of Materials Research, Materials Mechanics, Helmholtz-Zentrum Geesthacht, Max-Planck Straße 1, 21502 Geesthacht, Germany

ARTICLE INFO

Article history:
Received 22 May 2015
Revised 2 November 2015
Available online 2 December 2015

Keywords:
Nanocomposite
Metal-polymer composite
Extended crystal plasticity
Gold
Size effect

ABSTRACT

The impact of small scale geometric confinement on deformation mechanisms is subject of intense research in materials sciences nowadays. Nanoporous metals have a microstructure with an extremely high volume-specific surface content. Due to a very high local strength and a relatively regular interconnection of the nanoconstituents as well as a low mass density, nanoporous metals are very good candidates for strong and light-weight structural materials.

The modeling of a modern nanocomposite material of gold-polymer is in the focus of the contribution. A gradient extended crystal plasticity theory is applied to the computation of the mechanical response of the metal part of the composite and an elastic-viscoplastic continuum model is used for the simulation of the polymer material. The gradient hardening contribution is included into the crystal plasticity model in order to study the influence of the ligament size. Numerical results of the deformation of the gold-polymer nanocomposite under compression are presented. Simulation results are compared to the corresponding experimental data.

1. Introduction

Due to increasing significance of newly developed materials and/or materials with improved properties, material's characterization and simulation become more and more powerful tools. Recently, research on nanoporous metals significantly increased (Biener et al., 2008; Ding et al., 2004; Kramer et al., 2004; Saane et al., 2014; Wada and Kato, 2013; Wang and Weissmüller, 2013) due to their relatively high ductility and high specific strength. It has been shown that nanoporous metals exhibit size effects such as increasing strength with decreasing dimensions (Huber et al., 2014; Wang and Weissmüller, 2013). In case of nanoporous materials, it is the (ligament) size which matters. By ligament, we refer to the interconnected nano-/microstructural constituents. Of course, the material's response further depends on its nanoporous architecture. The gold-polymer composite considered in this contribution is hierarchical. To date, no established understanding of how to design a microstructured composite exists. As a consequence, there is a strong need for experimental as well as numerical studies at all scales.

This work aims at contributing to designing integrated nanostructured multiphase materials systems in which microstructure design enables strength. What happens at the small scale during deformation is amazingly complex as dislocation nucleation, dislocation starvation, capillary effects, lattice defects, size effects, among others, occur. As a consequence, the composite's mechanical properties differ greatly from those of the corresponding bulk materials.

This paper focuses on material modeling of a metal-polymer nanocomposite under large deformations, considering non-local effects via introduction of the plastic strain

* Corresponding author at: Institute of Continuum Mechanics and Material Mechanics, Hamburg University of Technology, Eißendorfer Str. 42, 21073 Hamburg, Germany. Tel.: +4917672306071; Fax: +4940428783428.
E-mail address: swantje.bargmann@tuhh.de (S. Bargmann).
URL: http://www.tuhh.de/icm (S. Bargmann)

http://dx.doi.org/10.1016/j.mechmat.2015.11.008

gradient into a crystal plasticity theory. [1] The modeling and analysis extends the experimental investigation of Wang and Weissmüller (2013) and this modeling approach allows to account for a bending dominated deformation behavior which, at this scale, results into a pronounced development of strain gradients. Extensive plastic localization is indeed expected for NPG as well as for polymer infiltrated composites. For the time being, we study its mechanical behavior at the lowest level and, therefore, do not take its hierarchy into account[2].

The metal part of the composite is a nanoporous gold. This material has intriguing material properties that show potential benefits for some applications due to its high specific surface area, high electrical conductivity, and reduced stiffness, see e.g., Balint et al. (2005); Balk et al. (2005); Volkert et al. (2006). The experimental investigations show a significant size effect in nano deformations of sub-micron gold (Greer et al., 2005; Volkert and Lilleodden, 2006). This effect can be modeled by application of an extended crystal plasticity theory, cf., e.g., Bardella (2006); Bargmann et al. (2011); Evers et al. (2004); Gurtin (2000); Kuroda and Tvergaard (2008); Lele and Anand (2008); Ohno and Okumura (2007). The model applied in the current contribution is based on Bargmann et al. (2011). Several different strain-hardening and strengthening phenomena exist in crystalline materials. One of the more important ones is latent hardening, i.e., an active slip system influences the hardening of a neighboring inactive slip system. It controls the shape of the single crystal yield surface. Among others, slip interactions and the development of geometrically necessary dislocations (GNDs) play a role in latent hardening. While there exist some experimental works on nanoporous metals (see above), there hardly are any with respect to nanoporous metal-polymer composites (Wang and Weissmüller, 2013), and even fewer deal with the computational modeling of their behavior.

Unlike crystalline materials, epoxy resin is an amorphous solid which appears in disordered form. Its stress response, when subjected to large monotonic plastic deformations, is rate dependent and highly nonlinear composed of a yield-peak, post-yield strain softening and rapid strain hardening where the post–yield stress softening is linked to the evolution of the local free-volume. Upon subsequent unloading, a Bauschinger-type reverse-yielding phenomenon is observed. A mathematical model which accounts for these observed phenomena, which is also applied in the current contribution is presented in Anand and Gurtin (2003), Gearing and Anand (2004). Regarding continuum elasto-viscoplastic theory uses the local free-volume associated with certain metastable states and the resistance to plastic flow as internal state variables. Using the dependence of the Helmholtz free energy on the plastic deformation gives rise to rapid strain-hardening subsequent to post-peak strain softening as well as a backstress in the flow rule.

[1] Although the here considered ligament sizes are within the nano scale (50–150 nm), the application of a continuum-based crystal plasticity model is justified by the fact that dislocation-starvation scenarios are not supported by corresponding results of Ngô et al. (2006) and, hence, do not apply to nanoporous gold.

[2] Continuum-mechanically based contributions on the simulation of size-effects in hierarchical structures can be found in, e.g., Bargmann et al. (2013); Scheider et al. (2015).

To gain further insight into the model, we take a detailed look at the predicted mechanical response of a two-dimensional representative volume element. The numerical implementation of the strongly coupled and nonlinear system of equations is realized with the finite element method in space and a mixed implicit-explicit integration procedure in time.

2. Material properties

2.1. Gold

Although gold is a rather exclusive material, it is of great interest in case of nanoporous metals as under compression it deforms up to large plastic strains (e.g., up to 120% true strain Wang and Weissmüller, 2013), whereas usually nanomaterials only allow for small deformations (Kumar et al., 2003). As observed in experiments, the strength of nanoporous gold crystals increases if crystal dimensions are reduced (Jin et al., 2009). Moreover, experiments show an intensive microstructure evolution in nanoporous gold during deformation and the interaction of dislocations with the surface (Wang and Weissmüller, 2013). The mechanical tests and the microstructure characteristics inferred from the electron backscatter diffraction (EBSD) suggest lattice dislocations to be the carriers of plastic deformation in nanoporous gold.

The experiments of Volkert and Lilleodden (2006) on single crystal sub-micron gold columns show the dependence of yield stress and apparent strain hardening rate on the column diameter. EBSD analyses revealed that nanoporous metals are polycrystalline with a grain size of $10\,\mu m$–$100\,\mu m$ (Wang and Weissmüller, 2013). Further, nanoporous gold exhibits a strong size effect at constant porosity, see the experimental data of Wang and Weissmüller (2013). These types of size effects motivate the design of nanocomposites - in order to take advantage and fine-tune their mechanical behavior. A recent study on the elastic and plastic Poisson's ratios of nanoporous gold during compression to large plastic strains is given in Lührs et al. (2016).

A Young's modulus of 79 GPa and Poisson's ratio of 0.44 are stated in, e.g., Balk et al. (2005); Jin et al. (2009); Volkert et al. (2006). The yield stress of sub-micron gold is in the range between 154 MPa and 560 MPa. The magnitude of the Burgers vector is approximately 0.2878 nm (Hull and Bacon, 2011).

2.2. Epoxy resin

Epoxy resin is a class of important engineering materials which is used in many areas of material design such as the production of different components of material systems featuring high static and dynamic loadability. Unlike gold, which is crystalline, epoxy resin is an amorphous solid which appear in a disordered form. The viscosity is very low, which is especially advantageous for infusion, protrusion and injection processes at temperatures between 10 °C and 50 °C. Pure epoxy specimens show elasto-plastic mechanical behavior during compressive loading. Their stress-strain behavior is highly nonlinear and typically involves three consecutive steps composed of a yield-peak, post-yield strain softening (especially at high temperatures) and rapid strain

hardening. Moreover, upon unloading after monotonic plastic deformation a Bauschinger-type reverse-yielding phenomena is observed. The plastic response of the material is also sensitive to the applied loading rate. The elasticity parameters of epoxy resin are as follows: a Young's modulus of 1.038 GPa, Poisson's ratio of 0.35, as well as the material density of 1.2 g/cm^3, the tensile strength of 60–75 MPa and the compressive strength of 80–90 MPa, see (Qi et al., 2005; Sul et al., 2014; Wang and Weissmüller, 2013). The initial yield stress is 28 ± 3 MPa (Wang and Weissmüller, 2013).

2.3. Gold-polymer composite

The metal-polymer composite consists of solid phase gold (ca. 30–40% volume fraction) and solid phase polymer, where nanoporous gold forms the basis. Despite its exclusiveness, gold is one of the preferred model materials for the design of nanocomposites as its ligament size is easily controlled during processing. Due to their extremely small structural size, the ligaments of nanoporous metals possess an extraordinary high local strength. The porous material is infiltrated with polymer. For details on the composite preparation, the reader is referred to Wang and Weissmüller (2013). During the infiltration with the polymer the metallic network is not deformed, however, it leads to ductilization. Quoting (Wang and Weissmüller, 2013) 'The interpenetrating nanocomposite material [...] exhibits a number of unusual and technologically attractive properties, specifically ductility in tension, the option of cold-forming, high electric conductivity and a strength significantly exceeding that of each of the constituent phases.'

Whereas the composite's mechanical response is isotropic at the millimeterscale, it is anisotropic at the nanoscale. Microstructural investigations show that the ligaments are of single crystal type and possess a disordered structure. Experimental data of Wang and Weissmüller (2013) clearly shows a ligament-size-dependent stress-strain behavior of nanoporous gold for ligament sizes from 15 nm to 150 nm. All samples demonstrate an elastic-plastic deformation behavior. Composite specimens with the smallest ligament size fail at less strain than those with larger ligaments, and also exhibit a somewhat larger sample-to-sample scatter in yield stress.

The resulting composite has a high strength as well as ductile behavior under tension. One interesting property is that the (Vickers) hardness of the composite is considerably higher than those of its components: hardness of composite (387 ± 14 MPa) > hardness of epoxy (129 ± 6 MPa) > hardness of NPG (33 ± 4 MPa) (Wang and Weissmüller, 2013). Further, for nanoporous gold as well as for the composite, the hardness increases with decreasing ligament size, cf. (Wang and Weissmüller, 2013).

3. Material modeling

The nanocomposite is modeled as a nanoporous single crystal filled with polymer. The kinematics are based on the multiplicative decomposition of the deformation gradient $\boldsymbol{F}$ into elastic and plastic parts as $\boldsymbol{F} = \boldsymbol{F}_\mathrm{e} \cdot \boldsymbol{F}_\mathrm{p}$ (Lee, 1969; Rice, 1971). The elastic Green–Lagrange strain tensor is defined as $\boldsymbol{E}_\mathrm{e} = 1/2[\boldsymbol{F}_\mathrm{e}^t \cdot \boldsymbol{F}_\mathrm{e} - \boldsymbol{I}]$ whose conjugate stress measure is the elastically rotated Cauchy stress $\boldsymbol{T}_\mathrm{e} = \boldsymbol{R}_\mathrm{e}^t \cdot \boldsymbol{T} \cdot \boldsymbol{R}_\mathrm{e}$ where the definition of the elastic rotation tensor $\boldsymbol{R}_\mathrm{e}$ requires the application of the polar decomposition theorem $\boldsymbol{F}_\mathrm{e} = \boldsymbol{R}_\mathrm{e} \cdot \boldsymbol{U}_\mathrm{e}$ with $\boldsymbol{U}_\mathrm{e}$ denoting the elastic right-stretch tensor. Further, deformations are studied with help of the right Cauchy–Green tensor $\boldsymbol{C}$

$$\boldsymbol{C} = \boldsymbol{F}^t \cdot \boldsymbol{F} = \boldsymbol{F}_\mathrm{p}^t \cdot \boldsymbol{C}_\mathrm{e} \cdot \boldsymbol{F}_\mathrm{p}, \tag{1}$$

the elastic right Cauchy–Green tensor $\boldsymbol{C}_\mathrm{e} = \boldsymbol{F}_\mathrm{e}^t \cdot \boldsymbol{F}_\mathrm{e}$, and the plastic left Cauchy–Green tensor $\boldsymbol{B}_\mathrm{p} = \boldsymbol{F}_\mathrm{p} \cdot \boldsymbol{F}_\mathrm{p}^t$. The relevant stress measures are the first Piola–Kirchhoff stress $\boldsymbol{P}$

$$\boldsymbol{P} = \boldsymbol{F}_\mathrm{e} \cdot \boldsymbol{S}_\mathrm{e} \cdot \boldsymbol{F}_\mathrm{p}^{-t} \tag{2}$$

and the second Piola–Kirchhoff stress $\boldsymbol{S}_\mathrm{e}$

$$\boldsymbol{S}_\mathrm{e} = \boldsymbol{F}_\mathrm{e}^{-1} \cdot \boldsymbol{\tau} \cdot \boldsymbol{F}_\mathrm{e}^{-t}. \tag{3}$$

Here, $\boldsymbol{\tau}$ is the Kirchhoff stress. The mechanical problem is governed by the balance of linear momentum

$$\boldsymbol{0} = \mathrm{Div}\boldsymbol{P} + \boldsymbol{b}_0, \tag{4}$$

where $\boldsymbol{b}_0$ is the body force.

3.1. Metal part: sub-micron sized gold

The deformation problem is linked to the microscopic behavior via the plastic velocity gradient tensor

$$\boldsymbol{L}_\mathrm{p} = \dot{\boldsymbol{F}}_\mathrm{p} \cdot \boldsymbol{F}_\mathrm{p}^{-1} = \sum_\alpha \nu_\alpha [\boldsymbol{s}_\alpha \otimes \boldsymbol{n}_\alpha], \tag{5}$$

where the slip rate ν_α, the slip direction $\boldsymbol{s}_\alpha$ and slip normal $\boldsymbol{n}_\alpha$ are introduced. The resolved shear stress is associated with the slip system α and defined as

$$\tau_\alpha = \boldsymbol{s}_\alpha \cdot \boldsymbol{M}_\mathrm{e} \cdot \boldsymbol{n}_\alpha, \tag{6}$$

where $\boldsymbol{M}_\mathrm{e} = \boldsymbol{C}_\mathrm{e} \cdot \boldsymbol{S}_\mathrm{e}$ is the Mandel stress.

Further, the free energy Ψ is introduced and additively split into an elastic (Ψ_e), a local hardening (Ψ_lh) and a gradient hardening (Ψ_gh) contribution. In particular, we choose

$$\Psi_\mathrm{e} := \frac{\mu}{2}[\boldsymbol{C}_\mathrm{e} - \boldsymbol{I}] : \boldsymbol{I} + \frac{\lambda}{2} \ln^2 J_\mathrm{e} - \mu \ln J_\mathrm{e},$$

$$\Psi_\mathrm{lh} := \frac{1}{2} \sum_{\alpha,\beta} H^\mathrm{l}_{\alpha\beta} \gamma_\alpha \gamma_\beta,$$

$$\Psi_\mathrm{gh} := \frac{1}{2} l^2 H^\mathrm{g} \sum_{\alpha,\beta} \big[\boldsymbol{b}_\alpha \cdot \boldsymbol{b}_\beta\big] g_{\mathrm{i}\alpha}\, g_{\mathrm{i}\beta}.$$

In these relations, $J_\mathrm{e} = \det \boldsymbol{F}_\mathrm{e}$ is the elastic Jacobian determinant, $H^\mathrm{l}_{\alpha\beta}$ denotes the local hardening matrix, and H^g is the gradient hardening modulus. l is an internal length scale parameter. Further, the following evolution equation for the geometrically necessary dislocations (GND) densities $g_{\mathrm{i}\alpha}$ is introduced (Bargmann et al., 2011 and Husser et al., 2014)

$$\dot{g}_{\mathrm{i}\alpha} = \sum_\beta \nu_\alpha \big[\boldsymbol{n}_\alpha \cdot \boldsymbol{s}_\beta\big] g_{\mathrm{i}\beta} - \frac{1}{b} \nabla_\mathrm{i} \nu_\alpha \cdot \boldsymbol{s}_\alpha. \tag{7}$$

Here and below, the index "i" refers to the intermediate configuration. b is the length of the Burgers vector $\boldsymbol{b}_\alpha = b\,\boldsymbol{s}_\alpha$. The first term accounts for latent hardening effects, i.e., the hardening of inactive slip systems due to active slip systems.

The viscoplastic (rate-dependent) flow rule is assumed as follows

$$v_\alpha = \frac{1}{t_*}\left[\frac{\langle \tau_\alpha - \kappa_\alpha - Y_\alpha\rangle}{C_0}\right]^m \text{ with } \langle x\rangle = \frac{1}{2}[x+|x|], \tag{8}$$

where the initial yield stress is denoted as Y_α and the micro-hardening stress κ_α, following (Ekh et al., 2007 and Ekh et al., 2011),

$$\kappa_\alpha = \frac{\partial \Psi}{\partial \gamma_\alpha} - \text{Div}\left(\frac{\partial \Psi}{\partial \nabla \gamma_\alpha}\right) \tag{9}$$

characterizes the material behavior in the plastic state. The relaxation time t_*, the drag stress C_0 and the rate sensitivity parameter m are the same for all slip systems. In the end, the formulation described above is in accordance with thermodynamic considerations, in which, the coupled field relation implies a dual hardening variable at the local level, having the character of a backstress. For further details, compare also the works of Bargmann and Ekh, 2013; Svendsen and Bargmann, 2010; Bargmann et al., 2010.

3.2. Polymer constituent: epoxy resin

The continuum theory for the elastic-viscoplastic deformation of epoxy resin used in the current work is due to[3] (Anand and Gurtin, 2003; Gearing and Anand, 2004). Besides the plastic deformation gradient, the internal state variables are the local free-volume η which is associated with certain metastable states and resistance to plastic flow s.

Analogously to the extended crystal plasticity theory, the Helmholtz free energy Ψ is additively decoupled into elastic Ψ_e and plastic Ψ_p parts. Ψ_e is formulated as

$$\Psi_e(\boldsymbol{E}_e) := \frac{1}{2}K[\text{tr}\boldsymbol{E}_e]^2 + \mu\ \text{dev}\boldsymbol{E}_e : \text{dev}\boldsymbol{E}_e, \tag{10}$$

where $K = E/3[1-2\nu]$ is the bulk modulus and $\mu = E/2[1+\nu]$ is the shear modulus with E being the Young's modulus and ν the Poisson's ratio. In amorphous materials, unlike in crystals, Ψ_p arises from an entropic contribution. In the light of statistical mechanics models of rubber elasticity, see, e.g., Treloar (1975); Arruda and Boyce (1993), Ψ_p has the following form

$$\Psi_p(\lambda_p) := \mu_R\lambda_L^2\left[\frac{\lambda_p}{\lambda_L}x + \log\left(\frac{x}{\sinh x}\right) - \frac{1}{\lambda_L}y - \log\left(\frac{y}{\sinh y}\right)\right], \tag{11}$$

with

$$x = \Gamma^{-1}\left(\frac{\lambda_p}{\lambda_L}\right) \quad \text{and} \quad y = \Gamma^{-1}\left(\frac{1}{\lambda_L}\right), \tag{12}$$

where $\lambda_p = \sqrt{\text{tr}\boldsymbol{B}_p/3}$ denotes the effective distortional plastic stretch. Γ^{-1} is the inverse of the Langevin function $\Gamma(z) = \coth(z) - 1/z$. μ_R and λ_L are the rubbery modulus and network locking stretch, respectively.

Using above forms, the equation for the stress is derived as follows

$$\boldsymbol{T}_e = \frac{\partial \Psi_e(\boldsymbol{E}_e)}{\partial \boldsymbol{E}_e} = K\text{tr}(\boldsymbol{E}_e)\boldsymbol{1} + 2\mu\text{dev}\boldsymbol{E}_e. \tag{13}$$

The dependence of Ψ_p on plastic deformation leads to a backstress $\boldsymbol{S}_{back}$ in the underlying flow rule which not only accounts for a Bauschinger-type reverse-yielding upon unloading after large plastic deformations but also controls the rapid strain-hardening response after the initial yield-drop

$$\boldsymbol{S}_{back} = 2\,\text{dev}\left(\text{sym}\left(\frac{\partial \Psi_p(\lambda_p)}{\partial \boldsymbol{B}_p}\cdot\boldsymbol{B}_p\right)\right) = \mu_{back}\,\text{dev}\boldsymbol{B}_p, \tag{14}$$

where μ_{back} denotes the backstress modulus

$$\mu_{back} = \frac{1}{3\lambda_p}\frac{\partial \Psi_p(\lambda_p)}{\partial \lambda_p} = \mu_R\frac{\lambda_L}{3\lambda_p}\Gamma^{-1}\left(\frac{\lambda_p}{\lambda_L}\right). \tag{15}$$

Since as $z\to 1$, $\Gamma^{-1}(z)\to\infty$, $\mu_{back}\to\infty$ as $\lambda_p\to\lambda_L$.

Using the plastic stretch tensor $\boldsymbol{D}_p = \text{sym}(\dot{\boldsymbol{F}}_p\cdot\boldsymbol{F}_p^{-1})$ one has $\dot{\boldsymbol{F}}_p = \boldsymbol{D}_p\cdot\boldsymbol{F}_p$ with $\boldsymbol{F}_p(\boldsymbol{X},0) = \boldsymbol{1}$. Noting that $\text{tr}\boldsymbol{T}_e = \text{tr}\boldsymbol{T}$, the flow rule defined for $\boldsymbol{D}_p$ reads

$$\boldsymbol{D}_p = v_p\left[\frac{\text{dev}\boldsymbol{T}_e - \boldsymbol{S}_{back}}{2\bar{\tau}}\right], \quad \text{where } v_p = v_0\left[\frac{\bar{\tau}}{s - \alpha 1/3\text{tr}\boldsymbol{T}_e}\right]^{1/n} \tag{16}$$

and $0 < n \le 1$ as well as $s - \alpha 1/3\text{tr}\boldsymbol{T}_e > 0$ are required, with α controlling the pressure sensitivity of the plastic flow. v_p is the equivalent plastic shear strain rate, v_0 the reference plastic shear strain rate, α and n the pressure and strain rate sensitivity parameter, respectively. The definition of the equivalent shear stress $\bar{\tau}$ reads

$$\bar{\tau} = \sqrt{\frac{1}{2}[\text{dev}\boldsymbol{T}_e - \boldsymbol{S}_{back}] : [\text{dev}\boldsymbol{T}_e - \boldsymbol{S}_{back}]}. \tag{17}$$

For $n\to 0$ rate-independent formulation is handled, whereas for $n\to 1$ linear viscosity is.

The isotropic resistance to plastic flow s and the local free volume η evolve according to

$$\dot{s} = v_p h_0\left[1 - \frac{s}{\tilde{s}(\eta)}\right] \quad \text{and} \quad \dot{\eta} = v_p g_0\left[\frac{s}{s_{cv}} - 1\right] \tag{18}$$

with $s(\boldsymbol{X},0) = s_0$ and s_0 representing the initial resistance to flow. In the virgin state of the material, free volume is assumed to vanish with $\eta(\boldsymbol{X},0) = 0$. Finally, $\tilde{s}$ is defined as

$$\tilde{s}(\eta) = s_{cv}[1 + b[\eta_{cv} - \eta]] \tag{19}$$

which concludes the set of equations defining the constitutive model for epoxy resin with $\{E, \nu, \alpha, n, s_{cv}, \eta_{cv}, b, h_0, v_0, g_0, s_0, \mu_R, \lambda_L\}$ constituting the set of the associated material constants to be identified.

[3] The reason for using an extended gradient theory for the gold and a classical local continuum formulation for the polymer is twofold: The first one is the relative compliance of polymer as compared to gold. Hence, the results of any corresponding second order effects are marginal once the overall composite behavior is concerned. The second reason is the lack of experiments at the scale of interest for pure epoxy.

Table 1
Model parameters for gold.

Parameter	Symbol	Value	Dimension
Local hardening modulus	H^{l}	10.2	[MPa]
Gradient hardening modulus	H^{g}	150.7	[MPa]
Relaxation time	t_*	10^3	[s]
Drag stress	C_0	1	[MPa]
Rate sensitivity parameter	m	20	[−]

4. Numerical parameter identification

4.1. Microcompression of gold single crystal

Single crystalline gold is under consideration in order to calibrate local and non-local hardening parameters based on microcompression investigations performed by Volkert and Lilleodden (2006). For this purpose, the numerical example is focused on two small micropillars with nominal diameters $D = 1$ μm and $D = 8$ μm. The internal length scale parameter for pure gold is taken to be $l = 1.5$ μm, in accordance with the argumentation of Begley and Hutchinson (1998) with respect to annealed and soft metals. The material parameters for gold are stated in Section 2.1, whereas the model parameters for the microcompression example are summarized in Table 1. For Young's modulus a value of 48 GPa is taken according to measurements in Volkert and Lilleodden (2006). This value differs from the expected value which is due to the fact that only grains with low symmetry orientation have been selected for pillar fabrication. In this orientation, a double slip configuration as illustrated in Fig. 1 was observed with slip directions s_α oriented with 37° and 31° wrt. to the compression axis leading to Schmid factors $f_1 = 0.48$ and $f_2 = 0.44$ respectively, cf. also Volkert and Lilleodden (2006). In this regard, latent hardening effects between both slip systems are addressed via the dislocation interaction term in Eq. (7).

In the experimental range of investigated sample sizes, the size dependence of the macroscopic yield stress $\bar{Y} = \bar{Y}(D)$ is approximated very well by the following power law in which the yield stress is directly connected to the nominal diameter of the sample:

$$\bar{Y} = 106.5 D^{-0.6}. \tag{20}$$

The resolved microscopic yield stress is then obtained as $Y_\alpha = f_\alpha \bar{Y}$ where f_α is the Schmid factor of the corresponding slip system.

The pillar geometry is approximated by a tapered cylinder having an aspect ratio of 2.8 and a taper angle of 2°. Furthermore, a base is considered in the model where the radius of curvature between the pillar and the base is set to be $D/4$ for both sample sizes. The complete FE-model consists of 11240 8-node hexahedral elements. The unknown field variables, i.e., the displacements and the GND densities, are interpolated using linear shape functions. Uniaxial compression load is applied via a rigid surface (not depicted in Fig. 1) under consideration of Coulomb friction. In analogy to Zhang et al. (2006), a friction coefficient of $\mu_{\mathrm{C}} = 0.03$ is assumed at the interface of the indenter and the pillar.

Due to the mechanical boundary conditions in the experiments, cf. also Husser et al., 2014, microhard conditions are assumed for the plastic slip rates at the horizontal boundaries, i.e., $\nu_\alpha \, \boldsymbol{N}^{(\mathrm{b})} \cdot \boldsymbol{s}_\alpha = 0$ on $\partial\mathcal{B}_{\mathrm{i}}^{\nu}$. All other boundaries are allowed to deform in the experiment which is captured by

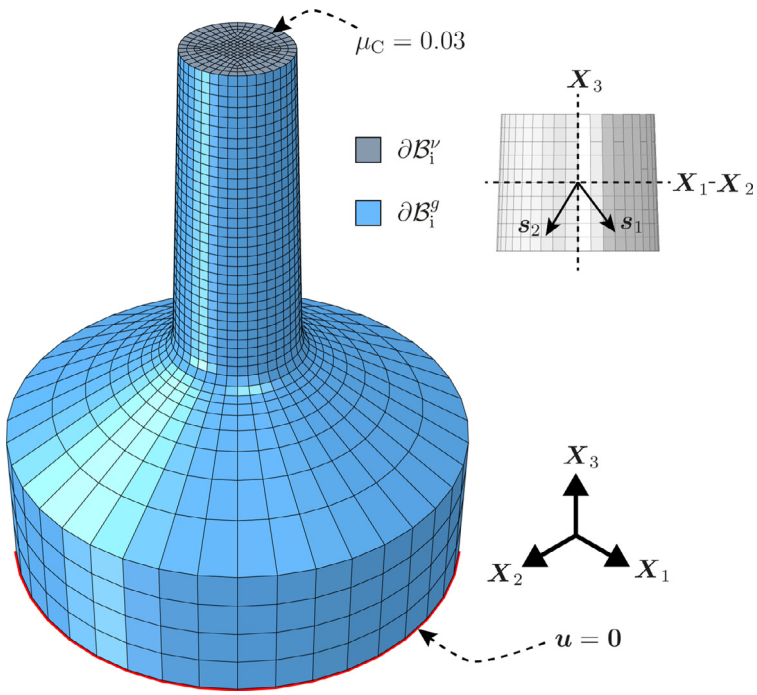

Fig. 1. FE-model of the representative gold micropillar including indication of different boundaries and illustration of the double slip configuration as considered in the numerical compression test.

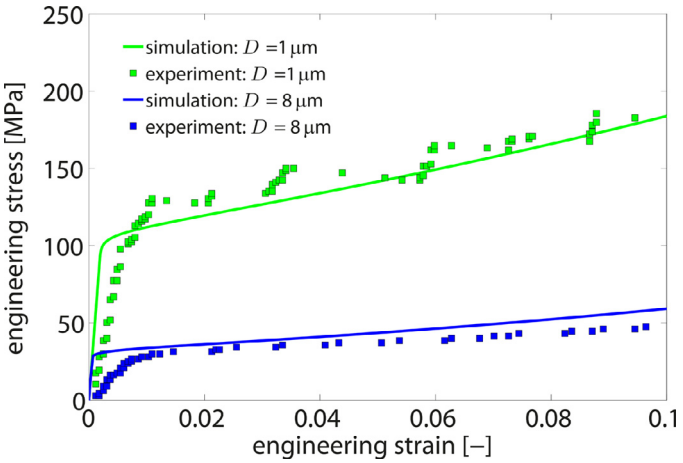

Fig. 2. Corresponding stress-strain curves are in good accordance with experimental data of Volkert and Lilleodden (Volkert and Lilleodden, 2006).

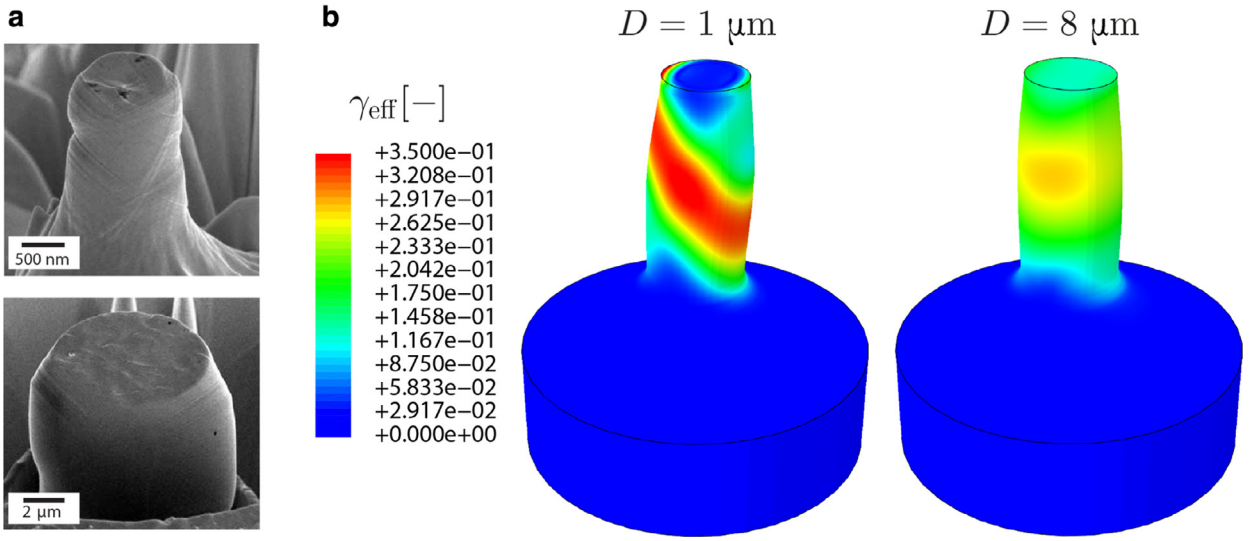

Fig. 3. (a) SEM images of deformed micro pillars (taken from Volkert and Lilleodden (2006)) and (b) corresponding contour plots of effective plastic slip $\gamma_{\text{eff}} = \sqrt{\sum_\alpha \gamma_\alpha^2}$. Results show that the gradient hardening effect is directly related to the deformation characteristic which is clearly more pronounced in the smaller sample in terms of a double slip band.

microfree conditions, i.e., $\dot{g}_{i\alpha} = 0$ on $\partial\mathcal{B}_i^g$. The two types of boundaries are indicated by a colormap in Fig. 1.

The stress-strain response for the compression test is presented in Fig. 2 and the deformation behavior is illustrated in Fig. 3. As expected and observed in corresponding experiments, the smaller sample shows a significantly higher gradient effect. This is reflected by the formation of a strongly pronounced double slip band, in accordance to experiments (Volkert and Lilleodden, 2006). Both slip bands are differently stressed: one slip system is more pronounced and hence accommodates more deformation.

4.2. Compression of bulk polymer

As a next step, a compression test of pure bulk polymer is modeled, in particular the one done by Wang and Weissmüller (2013). The sample has initial dimensions of 1 mm x 1 mm and is compressed from above with a constant engineering strain rate of $10^{-4}\,\text{s}^{-1}$. Since the test represents uniform field distributions, a single element is used in the evaluation of the stress response under axisymmetric compression where contraction free boundary conditions are devised. We use fixed values $\alpha = 0.204$, $\nu_0 = 0.0017\ \text{s}^{-1}$ and $n = 0.043$ for the strain-rate sensitivity parameter (Gearing and Anand, 2004; Rabinowitz et al., 1970). In identification of the remaining parameters $\{s_{cv}, \eta_{cv}, b, h_0, g_0, s_0, \mu_R, \lambda_L\}$, an optimization scheme with an objective function based on squared differences of the experimentally determined and simulated stress points corresponding to identical strains is applied. The list of the converged parameter set is given in Table 2. Fig. 4 displays the stress-strain response of the corresponding numerical example compared to the experimental data. The behavior is well-captured throughout the whole range of the analyzed monotonic deformation.

Table 2
Material parameters for the bulk epoxy resin.

Parameter	Symbol	Value	Dimension
Equilibrium value for s	s_{cv}	8.621	[MPa]
Equilibrium value for η	η_{cv}	0.000773	[−]
Parameter for $\tilde{s}$	b	1750.2	[−]
Rate controlling parameter for s	h_0	2147.8	[MPa]
Rate controlling parameter for η	g_0	0.004519	[−]
Reference plastic shear-strain rate	ν_0	0.0017	[s^{-1}]
Initial resistance to plastic flow	s_0	18.033	[MPa]
Pressure sensitivity parameter	α	0.204	[−]
Rate sensitivity parameter	n	0.043	[−]
Rubbery modulus	μ_R	5.2384	[MPa]
Network locking stretch	λ_L	1.67	[−]

5. Numerical study of gold-polymer composite

5.1. Mechanical behavior of the nanocomposite

The nanoporous gold-epoxy composite has a very complex structure, see Fig. 5(a). Numerical reconstruction of the real microstructure is too complex for such a detailed material model as presented in this contribution. As a consequence, we study a two-dimensional honeycomb structure as an idealization of the gold-polymer composite structure, cf. Fig. 5(b). Microstructural investigations show that in nanoporous gold the nanoscale pore network is contiguous, see, e.g., Fig. 5(a). Hence, the gold skeleton is referred to as open cell. In the selected plane strain configuration with its tunnel like microstructure, there exists a continuity in the

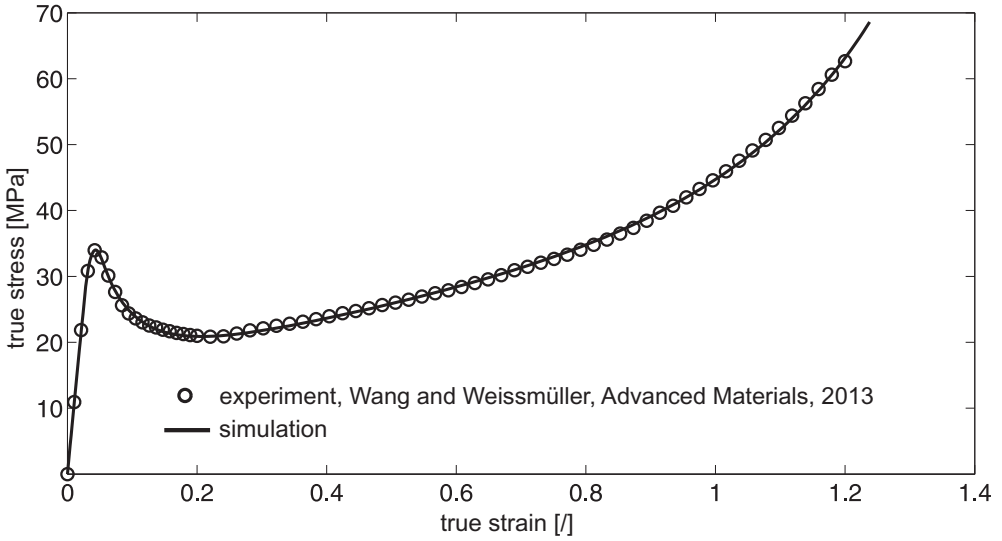

Fig. 4. Bulk polymer, compression test: Simulated stress-strain response and its comparison with the experimentally determined curve.

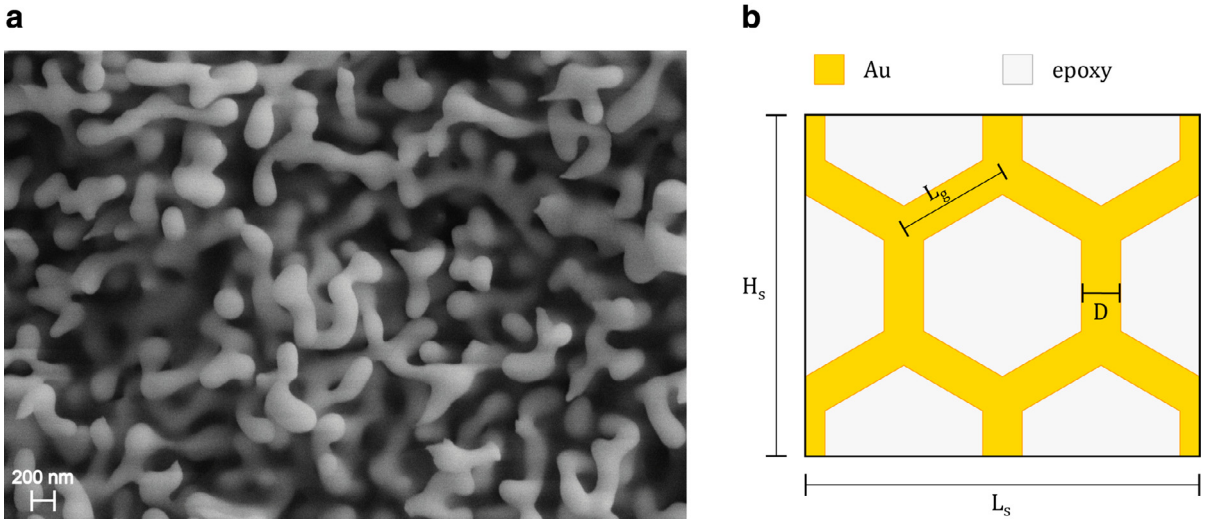

Fig. 5. Gold-polymer composite, (a): SEM picture of gold-epoxy composite with ligament size of 150 nm (kindly provided by K. Wang, Hamburg University of Technology), (b): Idealized two-dimensional honeycomb structure.

out of plane direction, but the gold hexagonal skeleton divides the domain into regular and isolated epoxy islands. This set-up of the honeycomb structure accounts for the influence of one gold ligament on the neighboring ones as well as the mutual influence of gold on polymer (and vice versa) during deformation.

Microstructural investigations show that the ligaments consist of single crystalline gold at the nanoscale. Thus, in all simulations, the gold phase of the representative volume element (RVE) consists of a single crystal. Together with applied periodic boundary conditions this amounts for a single crystal gold skeleton extending indefinitely in the plane. This assumption is reasonable due to observed crystallographic coherence of the ligaments at long range distances, see, e.g., Wang and Weissmüller (2013). The remaining material parameters of the constituents (gold and polymer) are the same as before.

Mimicking experiments, a compression test in vertical direction is simulated where with the selected configuration certain gold ligaments, henceforth called as the vertical ligaments, align along the loading direction. In order to distinguish the inclined ligaments from each other we name them as right- and left-inclined, respectively. If we tile the whole plane with the given microstructure, every junction is then a meeting point of three ligaments of distinct kinds, i.e., one vertical, one right- and one left-inclined. This level of order, as will be seen on the following lines, results in a comparatively stabilized response of the gold skeleton since in the actual microstructures a stochastic pattern is due. As will be shown later, the orientation of the ligaments relative to the loading direction is conclusive in the activated slip systems. The load is applied till a total of 20% true strain is carried out along the loading direction with a constant engineering strain rate of 10^{-3} s^{-1}. Periodic boundary conditions are applied to both fields, i.e., displacements and GND densities. For plastic slip, microfree boundary conditions are applied to the gold-polymer interface.

Taking the experimental data from Wang and Weissmüller (2013) as the basis, volume fractions of $\phi = 0.3$ and $\phi = 0.4$ and ligament diameters of 50 nm and 150 nm are used in the simulations. The developed modeling environment allows to investigate the influence of the gold content as well as the ligament diameter separately whereas, due to processing reasons, the samples of Wang and Weissmüller (2013) mix the influence of ligament diameter and gold fraction (composite 1: $D = 50$ nm and $\phi = 0.3$; composite 2: $D = 150$ nm and $\phi = 0.4$) and no separated influence was studied in their experiments.

During the whole loading history, ligaments whose directions coincide with the loading direction mainly deform under compression whereas the oriented ligaments mainly undergo in bending in addition to the compression. The resultant stress-strain responses projected in loading direction of composite structures with ligament diameter 50 nm resp. 150 nm and gold volume fraction of $\phi = 0.3$ resp. $\phi = 0.4$ are depicted in Fig. 6.

Due to the heterogeneous microstructure, the stress distributions are also heterogeneous. Hence, the stress components analyzed here are carried out through a standard homogenization procedure which accounts for mutual effects of gold and epoxy as load carrying agents. In this sense, the composite's response curve is a full outcome of the simulations and not an input. One can easily distinguish the characteristics of these curves as an initial elastic part, a yield point, an initial hardening branch, a slight post-peak softening and a subsequent mild plastic hardening region - which agrees very well with the reported experimental results of Wang and Weissmüller (2013) for $D = 150$ nm with $\phi = 0.4$ and $D = 50$ nm with $\phi = 0.3$. It should be noted, however, that unlike (Wang and Weissmüller, 2013), our results are in accordance with the rule of mixture. The variation of the volume fraction significantly influences the mechanical characteristics of the composite. Nevertheless, it should be noted that the comparison is made among nanostructures of identical topological properties. As given in the following subsection, authors' investigations show that, the connectivity at junctions and the size of the continuous load bearing ligament loops significantly affect the strength and stiffness. Hence, preserving volumetric content of gold while varying its connectivity might result in significantly different material response. At fixed ligament diameter, the composite with smaller gold fraction possesses a lower Young's modulus and

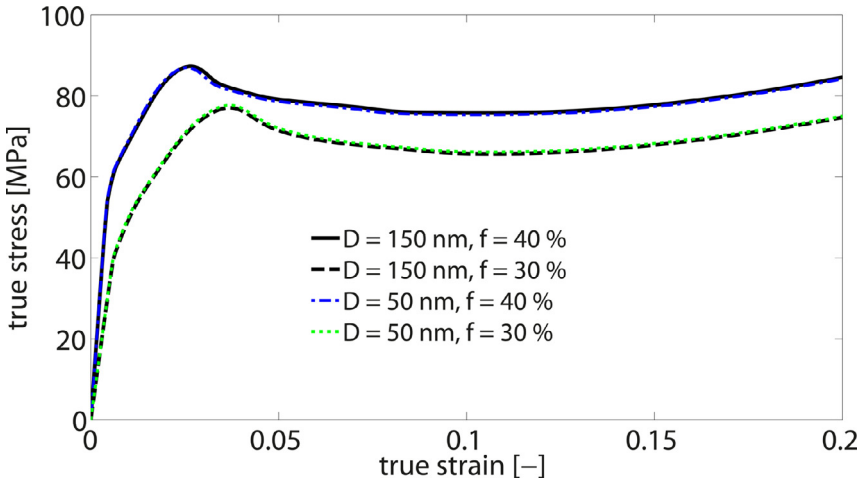

Fig. 6. Gold-polymer composite: influence of ligament diameter D and volume fraction ϕ on the stress-strain behavior.

a significantly lower yield stress. Mainly the gold content controls the yield stress. Ligament diameter on the other is effective on the hardening of the material. Initial hardening, post-peak softening and rehardening regions seem to be offsets of each other. Our investigations show that especially in the further stages of deformation, the rapid hardening of the epoxy is also effective in the increase in hardening rate under considerable compaction. The results recorded in the current study premise a gain in both strength and stiffness in composite response as compared to NPG or epoxy alone. This does not violate the rule of mixing taking into account that the pores in the gold skeleton are replaced by epoxy resin in the final composite structure.

The reason behind relatively higher predictions in flow stresses than the reported experiments could be attributed to the selected topological properties (perfect connectivity at the junctions) and to the reduction from three to two dimensions in the numerical compression test. This results in a tunnel like gold skeleton, which increases the structural stiffness. Here, the plane strain constraints govern through sufficiently limiting the admissible velocity space for the material flow, via, e.g., suppressed out of plane dislocation mobility. As a consequence, in the simulations the hardening regime following the post-peak softening occurs earlier and with larger plastic hardening modulus. For $D = 50$ nm the hardening is much weaker and even close to ideal plasticity within the simulated strain range. This is especially the case for increasing ligament diameter, where a size effect is clearly observed. Almost ideal plasticity results are carried out for $D = 150$ nm. Despite these minor differences, the analysis clearly shows the model's general capability to capture the material's mechanical response.

In Fig. 7, the distribution of the effective plastic slip $\gamma_{\text{eff}} = \sqrt{\sum_\alpha \gamma_\alpha^2}$ in the gold constituent at true strain of 20% is depicted in the deformed configuration. At this level of deformation, the maximum value of the effective plastic slip is found in the central region of the inclined ligaments for all gold contents and ligament sizes. Although there seems to be a balance in the effective plastic slips in the oriented ligaments, once the plastic slip in each slip system is observed different slip system dominate right- resp. left-inclined ligaments. This is anticipated taking the geometrically stiff and compliant directions of the inclined ligaments, the loading mode and the slip directions into account. As a consequence, in each inclined ligament the slip system with a direction transverse to the ligament axes produces more plastic flow whereas the ones with a direction along the ligament axis are relatively passive. One should note that with the approximate symmetry in distribution of the slip on inclined branches, extreme distortion of the microstructure under compression is suppressed and although periodic boundary conditions supply sufficient freedom in nodal displacements at the edges, the edges do not deviate too much and preserve their initial flatness. For the vertical ligaments, around the central region there exists a slightly oriented accumulation of plastic slip. However, the magnitude is not more than one third of the magnitude recorded in the inclined ligaments. In fact, at the very early stages of the deformation, at around 4 % of compression, this zone involves dominating effective plastic slip for $\phi = 0.3$ as depicted in Fig. 8. This shows that the microstructure has a tendency to deform in this more compliant bending mode as compared to the compression of vertical ligaments.

In Fig. 7, localized plasticity is clearly visible in the distribution of the plastic slip. Looking at the deformed figures and the contours of the effective plastic slip, it is clearly seen that (in agreement to what is noted in Wang and Weissmüller (2013) as compared to the individual plastic flow of the gold members) the volume changes of the RVE generally control the plastification. Of course, the volumetric changes in the RVE are limited by the epoxy impregnation as compared to a nanoporous gold structure.

For a constant gold volume fracture, it is observed that more plastic deformation takes place in ligaments with larger ligament diameter. In addition, a stronger localization in plastic deformation takes place for a constant diameter when increasing the volume fracture, leading to a stronger impact of GNDs on the material response. This is reflected by the increase of strength as shown by the stress-strain curve. Further, in the composite structures with a smaller ligament diameter, the accumulation of GNDs in regions with cross slip, i.e. in vertical ligaments, is strongly pronounced as illustrated in Fig. 9. This indicates that deformation is mostly carried in the inclined ligaments where single-slip is dominated. However, the accommodation of tensile/compression load of the vertical ligaments increases with reduced gold volume fracture as illustrated at an early state of deformation (4%) in Fig. 8. This direction holds at higher strain levels but is overlapped with strongly localized deformation in the inclined ligaments. In nanoporous gold, it is known that bending is the dominating deformation mode (Huber et al., 2014), whereas in epoxy enriched composites

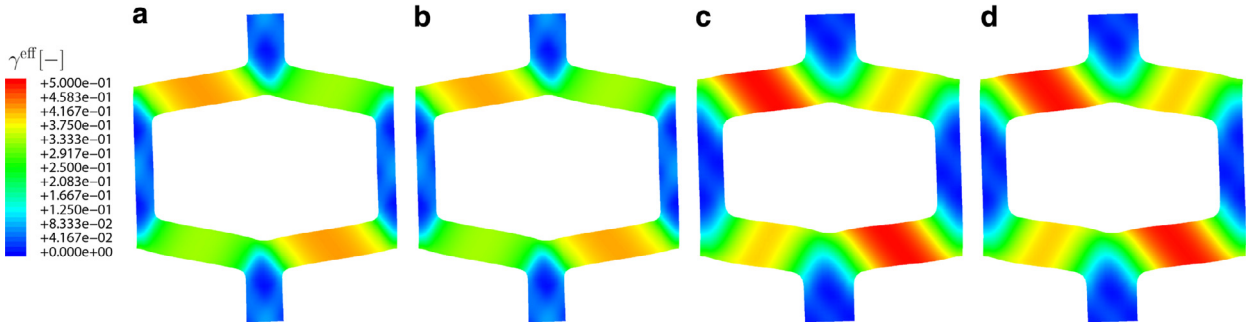

Fig. 7. Gold-polymer composite, gold constituent: effective plastic slip $\gamma_{\text{eff}} = \sqrt{\sum_\alpha \gamma_\alpha^2}$ distribution at 20% true strain for (a) $\phi = 0.3$, $D = 50$ nm, (b) $\phi = 0.3$, $D = 150$ nm, (c) $\phi = 0.4$, $D = 50$ nm and d) $\phi = 0.4$, $D = 150$ nm.

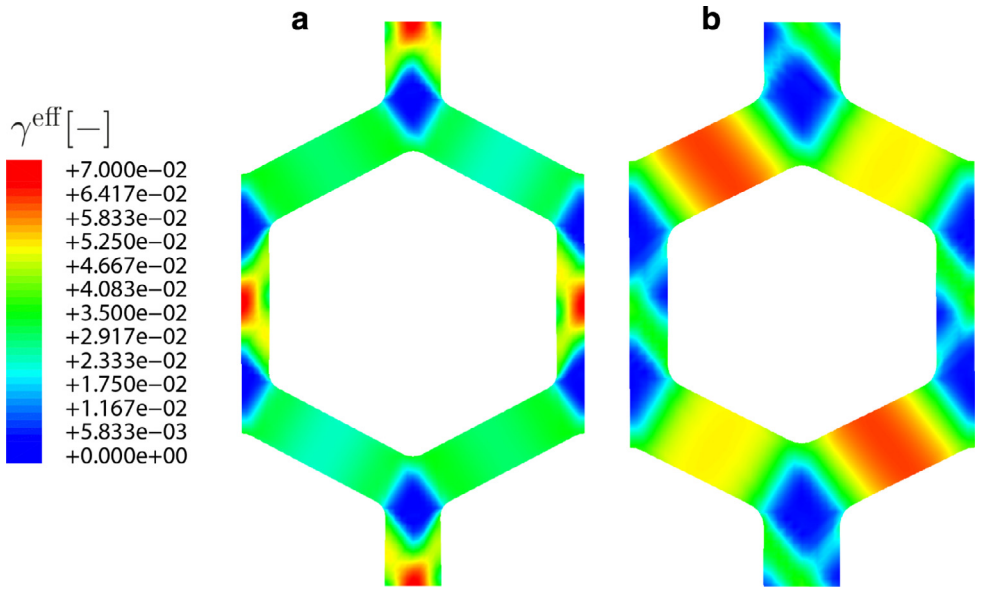

Fig. 8. Gold-polymer composite, gold constituent: effective plastic slip $\gamma_{\mathrm{eff}} = \sqrt{\sum_\alpha \gamma_\alpha^2}$ distribution at 4% true strain for $D = 150$ nm, (a) $\phi = 0.3$ and (b) $\phi = 0.4$. The influence is clearly seen in the distribution of the effective plastic slip. We also observe that plastic deformation is carried by vertical ligaments up to a deformation of approximately 4% in case of $\phi = 0.3$.

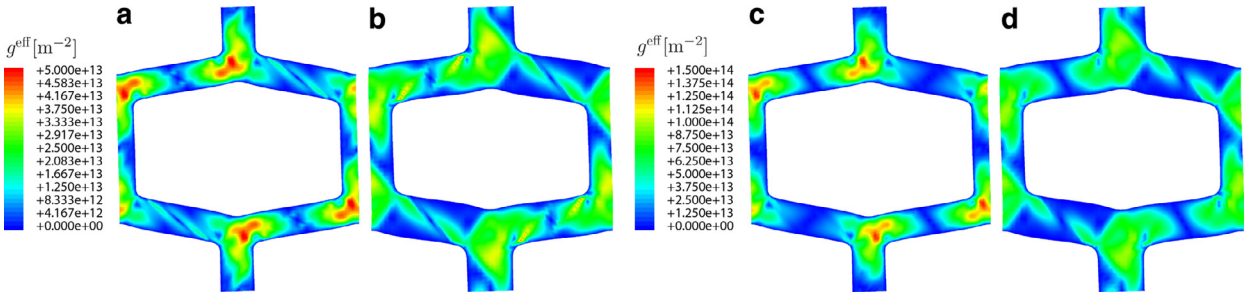

Fig. 9. Gold-polymer composite, gold constituent: GND density distribution at 20% true strain for (a) $\phi = 0.3$, $D = 50$ nm, (b) $\phi = 0.4$, $D = 50$ nm, (c) $\phi = 0.3$, $D = 150$ nm and (d) $\phi = 0.4$, $D = 150$ nm. The size effect is clearly seen in the distribution of effective GND density.

a mixture of tension/compression and bending is typically observed.

The arrangement in the selected microstructure where each junction hosts a vertical and two inclined ligaments effectively eliminates many collapse scenarios except for two: the first one being a snap through buckling of the oriented ligaments or buckling and/or shear banding in the vertical ligaments. The deformation patterns show that, with the selected topology, it is highly unlikely that the latter mechanism precede the former. In agreement with experimental observations, the loading of the composite in simulations can be proceeded until large deformations without a severe localization or collapse mechanism observed. Here, the positive effect of epoxy on the gold skeleton should not be overlooked. In view of the envisaged collapse scenarios, the epoxy resin surrounding the gold skeleton has two apparent advantages. Initially, for vertical ligaments they increase the Euler buckling load, stabilizing the effective length of the gold columns. Secondly but more importantly, the epoxy resin brings an additional stiffness to stabilize the collapse of the microstructure through a snap through buckling of the oriented ligaments. This is in agreement with the observations of Wang and Weissmüller (2013) on nanoporous gold composites where the impregnation through bringing control to the active volume change, increases stability of the system. Also it is noted that the bending modes are converted to the normal loading patterns, a scenario which is not in complete agreement with the simulations. Hence, we see that the major mechanisms are not altered but the intensities are changing.

Fig. 10 illustrates the evolution of the plastic deformation (the 22-component of $\boldsymbol{F}_{\mathrm{p}}$) in the epoxy resin for the composite with ligament diameter 50 nm and gold fraction 0.3. In terms of the mechanical behavior, the characteristics are the same for both ligament sizes and both gold fractions. Quantitatively, they differ, i.e., the size effect also affects the epoxy. The main compression mechanism is controlled by the compression of epoxy and bending of the oriented ligaments. This brings a considerable shortening in the epoxy fibers along central junction points of the gold ligaments where maximum shortening takes place at the very center. Epoxy material points in contact with the vertical gold ligaments are

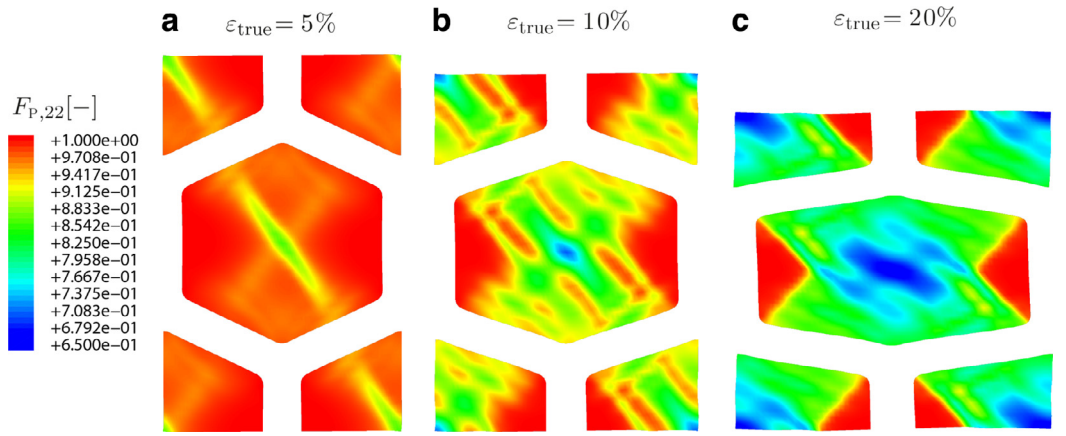

Fig. 10. Gold-polymer composite ($D = 50$ nm, $\phi = 0.3$), epoxy constituent: Evolution of plastic deformation (22-component of $\boldsymbol{F}_{\text{p}}$) at different levels of deformation with true strains of (a) 5%, (b) 10% and (c) 20%.

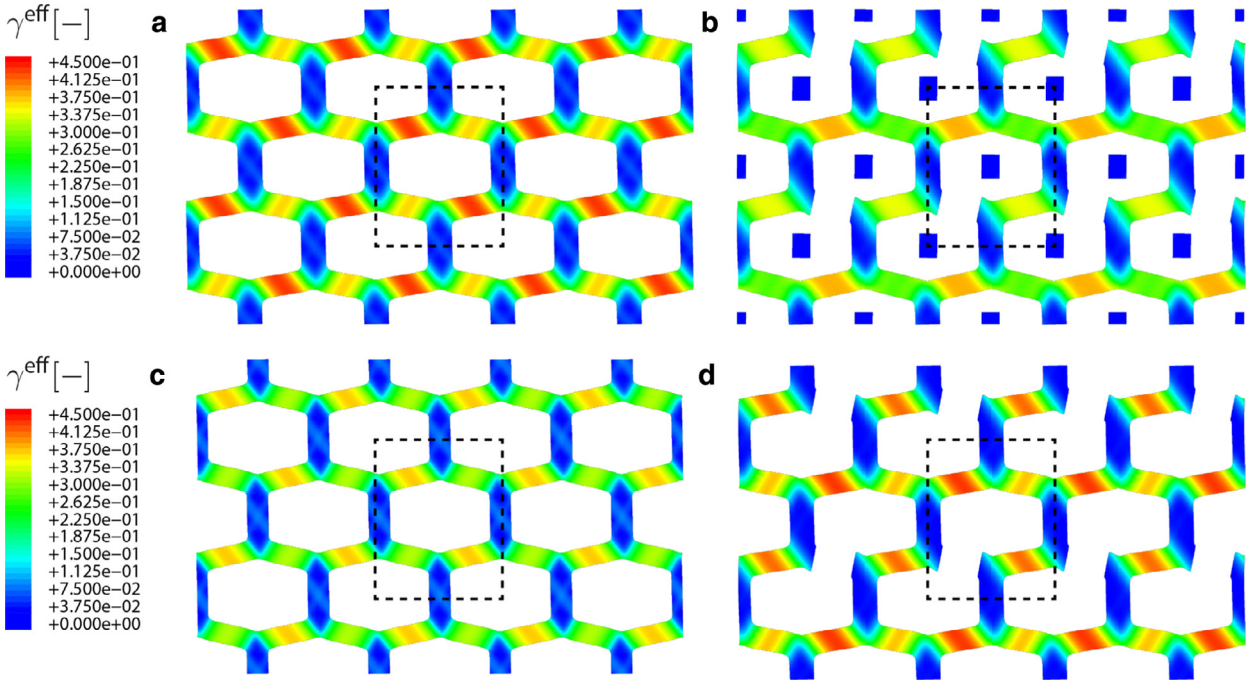

Fig. 11. Accommodation of plasticity for different variations of the cell structure: (a) regular unit cell, $\phi = 0.4$; (b) open unit cell with inclusions, $\phi = 0.4$; (c) regular unit cell, $\phi = 0.35$; (d) open unit cell, $\phi = 0.35$. The ligament size $D = 150$ nm is constant for all cases.

least compressed. This preserved region gradually dissolves towards the center. This is clearly depicted in the plastic deformation gradient plots for the loading direction. Maximum deviation from unity, which represents maximum plastic deformation, happens to take place in the center. This region is also the location of maximum elongated fibers in the transverse direction and with the highest von Mises stress at the end of the loading. During monotonic compression of the RVE, the material regions around the inclined ligaments plastify first. Then, rapidly with an arc-like effect this maximum plastic flow region is carried over to the center. During plastic flow, the material points first experience plastic hardening during initial yielding. Once the peak is reached, they unload due to softening controlled by the free volume of the epoxy. Later on with further plastic deformation, rapid hardening is attained which adds up to the composite's strength.

5.2. Variation of the cell structure - effect of ligament connectivity

The ligament network of gold-polymer composite reveals a low ligament connectivity density for larger ligament sizes. As a consequence, broken ligaments in larger ligament sizes might lead to an additional influence of the initial stiffness as well as the strength of the composite as they lead to (locally) larger load-bearing zones. The deformed structures are illustrated in Fig. 11 at a true strain level of 10%. From left to right and from top to bottom their respective characteristics

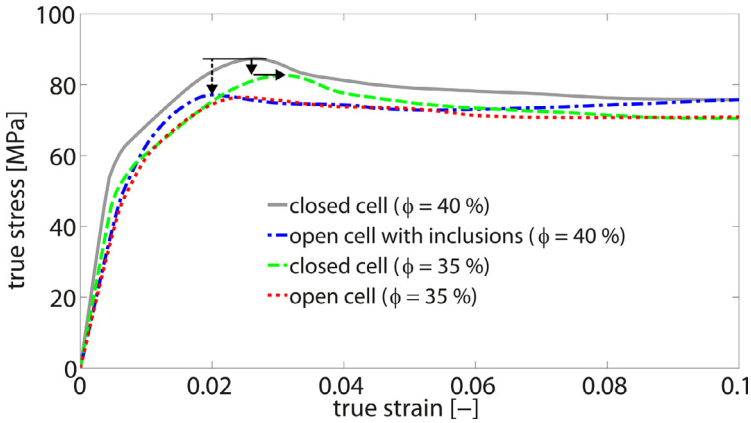

Fig. 12. Stress-strain curves of corresponding cell structures presented in Fig. 11.

are: (a) closed (regular) unit cell with $\phi = 0.4$; (b) open unit cell with inclusions and $\phi = 0.4$; (c) closed unit cell with $\phi = 0.35$; (d) open unit cell with $\phi = 0.35$. For all cases, the same ligament size of D = 150 nm is considered in order to eliminate any size-dependent influences stemming from the gold.

The corresponding stress-strain curves are presented in Fig. 12. For improved comparability, the elastic tangent is extended in the diagram. One can find a decrease in stiffness with decreasing gold volume fraction for the same connectivity density (cf. grey and green curves). The same tendency is presented for various ligament sizes and for a wide range of solid volume fractions in the recent work of Mameka et al. (2015). Besides, it can be seen that the overall composite strength reduces together with a drop in the peak stress which additionally is shifted towards a higher strain level. Keeping the gold volume fraction constant and reducing the connectivity density - archived by braking off one ligament connection - indicates a further decrease in stiffness (cf. green and red curves). Here, the resulting increase in load-bearing zones results in a softer response of the composite, noticeable in the matter of a further reduced peak stress. Finally, it should be noted, that unconnected inclusions influence the stiffness as well as the strength only slightly since such unloaded ligament segments do not accommodate any deformation (cf. red and blue curves). Consequently, their volume fraction of 5% does not follow the above mentioned trend. Of course the loss of structural symmetry in the newly constructed models has consequences on the model response. Still, even if the symmetry is preserved, completely unconnected ligaments (less likely in NPG) or ligaments with dead ends (more likely in NPG) accommodate considerably less plasticity hence the topological effect persists.

6. Conclusions

It is well understood that a material's microstructure might strongly influence its macroscopic deformation behavior (though it is not always fully understood 'how'). One direction in materials science is to specifically design a material's microstructure and, by this, improve its properties. As gold is quite an exclusive metal component for the composite, there already exists research towards a less noble constituent, see e.g., the works on macroporous iron, chromium and ferritic stainless steel (Wada and Kato, 2013), nanoporous titan (Wada et al., 2011), or copper (Hayes et al., 2006).

Our work contributes to the development of nanoporous metal-polymer composites, where particularly the gold's microstructure is of interest and varied during the preparation process. Due to the small size of the gold ligaments and the filling polymer constituents, the interfacial area is drastically larger compared to standard materials.

In the current contribution, the elastic-viscoplastic deformation of the gold-polymer nanocomposite under compressive loading is investigated in the framework of extended continuum mechanics. The crystalline behavior is modeled via a gradient extended crystal plasticity theory which captures the size effect (of bulk gold as well as of the composite), latent hardening and the Bauschinger effect. The amorphous polymer behavior is modeled using a phenomenological visco-plastic theory which accounts for local free volume, which is associated with certain metastable states. The model not only accounts for a Bauschinger-type reverse-yielding upon unloading after large plastic deformations but also controls the rapid strain-hardening response after the initial yield-drop. The qualitative hardening behavior of the composite is well mapped. To date, ideal contact between gold and polymer is assumed. Further, the strengthening by interfacial phenomena is not captured by the model yet, although it is anticipated to influence the mechanical behavior. Both are part of ongoing research.

The developed modeling environment allows investigation of separated influence of the gold content as well as the ligament diameter whereas, due to processing reasons, no separated influence can be studied in the experiments of Wang and Weissmüller (2013). With the current study we show that the macroscopic response curves carried out with the conducted simulations qualitatively agree very well with the experimental findings. The characteristics of these curves as an initial elastic part, a yield point, an initial hardening branch, a slight post-peak softening and a subsequent mild plastic hardening region are well captured. Our investigations also show that ligament connectivity has a large

influence on material's strength and stiffness. This could explain the inadequacy of the application of the rule of mixture in various applications with nanoporous gold composites.

Acknowledgments

We gratefully acknowledge financial support from the German Research Foundation (DFG) via SFB 986 "M^3", project B6. Fruitful discussions within the SFB, in particular (but not exclusively) with N. Huber, K. Wang and J. Weissmüller are also gratefully acknowledged.

References

Anand, L., Gurtin, M.E., 2003. A theory of amorphous solids undergoing large deformations, with application to polymeric and metallic glasses. Int. J. Solids Struct. 40, 1465–1487.
Arruda, E.M., Boyce, M.C., 1993. A three-dimensional constitutive model for the large stretch behavior of rubber elastic materials. J. Mech. Phys. Solids 41, 389–412.
Balint, D.S., Deshpande, V.S., Needleman, A., 2005. A discrete dislocation plasticity analysis of grain-size strengthening. Mater. Sci. Eng.: A 186, 400–401.
Balk, T.J., Eberl, C., Sun, Y., Hemker, K.J., Gianola, D.S., 2005. Tensile and compressive microspecimen testing of bulk nanoporous gold. JOM: The Memb. J. Miner. Metals and Mater. Soc. 61 (12), 26.
Bardella, L., 2006. A deformation theory of strain gradient crystal plasticity that account for geometrically necessary dislocations. J. Mech. Phys. Solids 54, 128.
Bargmann, S., Ekh, M., 2013. Microscopic temperature field prediction during adiabatic loading in a gradient extended crystal plasticity theory. Int. J. Solids Struct. 50, 899.
Bargmann, S., Ekh, M., Runesson, B., Svendsen, B., 2010. Modeling of polycrystals with gradient crystal plasticity - a comparison of strategies. Philos. Mag. 90 (10), 1263.
Bargmann, S., Scheider, I., Xiao, T., Yilmaz, E., Schneider, G., Huber, N., 2013. Towards bio-inspired engineering materials: Modeling and simulation of the mechanical behavior of hierarchical bovine dental structure. Comput. Mater. Sci. 79, 390.
Bargmann, S., Svendsen, B., Ekh, M., 2011. An extended crystal plasticity model for latent hardening in polycrystals. Comp. Mech. 48, 631.
Begley, M.R., Hutchinson, J.W., 1998. The mechanics of size-dependent indentation. J. Mech. Phys. Solids 46, 2049–2068.
Biener, J., Hodge, A.M., Hamza, A.V., 2008. Deformation Behavior of Nanoporous Metals, in Micro- and Nanomechanical Testing of Materials and Devices. Springer.
Ding, Y., Kim, Y.-J., Erlebacher, J., 2004. Nanoporous gold leaf: ancient technology/advanced materials. Adv. Mater. 16 (21), 1521.
Ekh, M., Bargmann, S., Grymer, M., 2011. Influence of grain boundary conditions on modeling of size-dependence in polycrystals. Acta Mechanica 218 (1-2), 103.
Ekh, M., Grymer, M., Runesson, K., Svedberg, T., 2007. Gradient crystal plasticity as part of the computational modelling of polycrystals. Int. J. Numer. Methods in Eng. 72, 197.
Evers, L.P., Brekelmans, W.A.M., Geers, M.G.D., 2004. Non-local crystal plasticity model with intrinsic ssd and gnd effects. J. Mech. Phys. Solids 52, 2379.
Gearing, B.P., Anand, L., 2004. On modeling the deformation and fracture response of glassy polymers due to shear-yielding and crazing. Int. J. Sol. Struct. 41, 3125.
Greer, J.R., Oliver, W.C., Nix, W.D., 2005. Size dependence of mechanical properties of gold at the micron scale in the absence of strain gradients. Acta Materialia 53 (6), 1821.
Gurtin, M., 2000. On the plasticity of single crystals: free energy, microforces, plastic-strain gradient. J. Mech. Phys. Solids 48, 989.
Hayes, J.R., Hodge, A.M., Biener, J., Hamza, A.V., Sieradzki, K., 2006. Monolithic nanoporous copper by dealloying mncu. J. Mater. Res. 21 (10), 2611.
Huber, N., Viswanath, R.N., Mameka, N., Markmann, J., Weißmüller, J., 2014. Scaling laws of nanoporous metals under uniaxial compression. Acta Materialia 67, 252.
Hull, D., Bacon, D.J., 2011. Introduction to Dislocations. Elsevier.
Husser, E., Lilleodden, E., Bargmann, S., 2014. Computational modeling of intrinsically induced strain gradients during compression of c−axis-oriented magnesium single crystal. Acta Materialia 71, 206.
Jin, H.J., Kurmanaeva, L., Schmauch, J., Rösner, H., Ivanisenko, Y., Weißmüller, J., 2009. Deforming nanoporous metal: Role of lattice coherency. Acta Materialia 57, 2665.
Kramer, D., Viswanath, R.N., Weissmüller, J., 2004. Surface-stress induced macroscopic bending of nanoporous gold cantilevers. Nano Lett. 4 (5), 793.
Kumar, P.S., Ramachandra, S., Ramamurty, U., 2003. Effect of displacement-rate on the indentation behavior of an aluminum foam. Mater. Sci. Eng.: A 347, 330.
Kuroda, M., Tvergaard, V., 2008. On the formulations of higher-order strain gradient crystal plasticity models. J. Mech. Phys. Solids 56, 1591.
Lee, E.H., 1969. Elastic-plastic deformation at finite strains. J. Appl. Mech. 36, 1.
Lele, S.P., Anand, L., 2008. A small-deformation strain-gradient theory for isotropic viscoplastic materials. Philos. Mag. 88, 3655.
Lührs, L., Soyarslan, C., Markmann, J., Bargmann, S., Weissmüller, J., 2016. Elastic and plastic poisson's ratio of nanoporous gold. Scripta Materialia 110, 65–69.
Mameka, N., Wang, K., Markmann, J., Lilleodden, E.T., Weissmller, J., 2015. Nanoporous goldtesting macro-scale samples to probe small-scale mechanical behavior. Mater. Res. Lett. 1–10.
Ngô, B.-N. D., Stukowski, A., Mameka, N., Markmann, J., Albe, K., Weissmüller, J., 2006. Anomalous compliance and early yielding of nanoporous gold. Acta Materialia 93, 144–155.
Ohno, N., Okumura, D., 2007. Higher-order stress and grain size effects due to self energy of geometrically necessary dislocations. J. Mech. Phys. Solids 55, 1879.
Qi, D., Hinkley, J., He, G., 2005. Molecular dynamics simulation of thermal and mechanical properties of polyimidecarbon-nanotube composites. Modell. Simul. Mater. Sci. Eng. 13 (4), 493.
Rabinowitz, S., Ward, I.M., Parry, J.C., 1970. The effect of hydrostatic pressure on the shear yield behavior of polymers. J. Mater. Sci. 5, 29–39.
Rice, J., 1971. Inelastic constitutive relations for solids: an internal variable theory and its application to metal plasticity. J. Mech. Phys. Solids 19, 433.
Saane, S.S.R., Mangipudi, K.R., Loos, K.U., De Hosoon, J.M., Onck, P.R., 2014. Multiscale modeling of charge-induced deformation of nanoporous gold structures. J. Mech. Phys. Solids 66, 1.
Scheider, I., Xiao, T., Yilmaz, E., Schneider, G., Huber, N., Bargmann, S., 2015. Damage modelling of small scale experiments on dental enamel with hierarchical microstructure. Acta Biomaterialia 15, 244–253.
Sul, J.H., Prusty, B.G., Kelly, D.W., 2014. Application of molecular dynamics to evaluate the design performance of low aspect ratio carbon nanotubes in fibre reinforced polymer resin. Composites: Part A 65, 64.
Svendsen, B., Bargmann, S., 2010. On the continuum thermodynamic rate variational formulation of models for extended crystal plasticity at large deformation. J. Mech. Phys. Solids 58, 1253.
Treloar, L.R.G., 1975. The Physics of Rubber Elasticity. Oxford.
Volkert, C., Lilleodden, E., 2006. Size effect in the deformation of sub-micron au columns. Philos. Mag. 86, 5567.
Volkert, C., Lilleodden, E., D., K., Weissmüller, J., 2006. Approaching the theoretical strength in nanoporous au. Appl. Phys. Lett. 89, 061920.
Wada, T., Kato, H., 2013. Three-dimensional open-cell macroporous iron, chromium and ferritic stainless steel. Scripta Materialia 68 (9), 723.
Wada, T., Setyawan, A.D., Yubuta, K., Kato, H., 2011. Nano- to submicroporous -ti alloy prepared from dealloying in a metallic melt. Scripta Materialia 65 (6), 532.
Wang, K., Weissmüller, J., 2013. Composites of nanoporous gold and polymer. Adv. Mater. 25, 1280.
Zhang, H., Schuster, B.E., Wei, Q., Ramesh, K.T., 2006. The design of accurate micro-compression experiments. Scripta Materialia 54 (2), 181.